

Alloy Formation and Surface Segregation in Zeolite-Supported Pt–Pd Bimetallic Catalysts

Poul L. Hansen,^{*,†} Alfons M. Molenbroek,^{†,‡} and Andrei V. Ruban[‡]

Haldor Topsøe Research Laboratories, Nymøllevej 55, DK-2800 Lyngby, Denmark, and
Center for Atomic-Scale Materials Physics and Physics Department, Technical University of Denmark,
DK-2800 Lyngby, Denmark

Received: September 10, 1996; In Final Form: November 25, 1996[⊗]

We present extended X-ray absorption fine structure (EXAFS) and transmission electron microscopy (TEM) measurements on three zeolite-supported bimetallic Pt–Pd catalysts prepared by wet impregnation. Alloy formation and segregation of Pd to the surface of the small bimetallic particles is clearly identified. Ab initio LMTO calculations are used to predict segregation profiles of low-index single-crystal Pt–Pd alloy surfaces. Pd is found to be enriched at the surface. EMT potentials for Pt and Pd are adjusted in order to give the same segregation profiles at low-index single-crystal surfaces as linear muffin tin orbital (LMTO) calculations. Monte Carlo simulations based on the adjusted EMT potentials are then used to calculate the equilibrium structure of small bimetallic Pt–Pd particles. Coordination numbers derived from these equilibrium structures are compared with those derived from EXAFS analysis, and a good agreement is found.

I. Introduction

Catalysis on supported metals plays a very important role in the chemical and petrochemical industries. Catalysts based on a single metal are used in such processes as steam reforming of methane where a synthesis gas mixture of CO and H₂ is produced over a supported Ni catalyst. Supported Cu is used for synthesis of methanol, and highly dispersed Pt and Pd is used for various oxidation, hydrogenation, and dehydrogenation reactions involving hydrocarbons.¹ The catalytic activity of supported metals may often be improved by addition of small amounts of other metals such as alkali metals or by completely alloying with another metallic element. Examples of industrial bimetallic catalyst are Pt–Sn, which is used for reforming of naphtha, and Pt–Pd for hydrogenation of aromatics in diesel oil.² Much effort is presently being invested in the understanding of the reactivity of metal alloy surfaces.³ Recently, theoretical models have predicted the interaction between simple molecules (H₂ and CO) and alloy surfaces (NiAl)⁴ and experimental work on surface alloys prepared on single-crystal surfaces (e.g., Pt–Sn) has shown that both activity and selectivity in hydrocarbon reactions are strongly influenced by the amount and detailed position of Sn on the Pt surface.^{5,6}

The present study deals with characterization of Pt–Pd catalysts supported on HY-zeolite where we address the question of alloy formation and surface composition in the small metallic particles. Sinfelt^{7,8} introduced the concept of bimetallic clusters and emphasized their potential as catalysts by showing how activity and selectivity of single metal catalysts could be modified by alloying with another element. Using the extended X-ray absorption fine structure (EXAFS) technique and chemisorption of probe molecules for characterization, alloy formation was observed, and it was even possible in some cases (Cu–Ru catalysts) to show that one element (Cu) segregated to the surface of the bimetallic particles leaving a core of the second metal (Ru). In the Pt–Pd system alloy formation and segregation of Pd to the surface of the bimetallic particles has been observed using EXAFS and transmission electron microscopy (TEM).⁹ In this particular case, the Pt–Pd particles were

prepared as polymer protected colloids and used as such in low-temperature hydrogenation of 1,3-octadiene.

The EXAFS technique provides information on the average coordination number of each element in the alloy. In the case of Pt–Pd alloys, X-ray absorption spectra were recorded at the Pt L₃-edge and the Pd K-edge. From the Pt L₃-edge data, the average number of Pt–Pt ($N_{\text{Pt-Pt}}$) and Pt–Pd ($N_{\text{Pt-Pd}}$) nearest-neighbors around a Pt atom is obtained by a curve-fitting procedure. The Pd K-edge data provide similar information for the average local environment of the Pd atoms in the sample, i.e., $N_{\text{Pd-Pd}}$, the average number of Pd nearest-neighbors and $N_{\text{Pd-Pt}}$, the average number of Pt nearest-neighbors. A common procedure to deduce a structural model for the bimetallic clusters from the four coordination numbers is to estimate a value for the average particle size, assume a particle shape, (e.g. spherical or truncated octahedron) and neglect the possibility of a variation in the composition of the particles. In a random alloy, all 4 coordination numbers are expected to be equal while in the case of segregation of Pd to the surface $N_{\text{Pd-Pd}}$ is expected to be “low” and $N_{\text{Pt-Pt}}$ is expected to be “high”.

In the present study, we provide structural information on zeolite supported Pt–Pd particles prepared by an impregnation technique. We use the EXAFS and TEM techniques and include variations in particle size and composition in our interpretation of the EXAFS coordination numbers. This is done by studying a series of samples with different Pd:Pt ratios, by measuring the actual particle size distribution using TEM, and by comparing the coordination numbers from EXAFS with coordination numbers obtained from calculated equilibrium structures of Pt–Pd particles of different sizes and compositions. The prediction of equilibrium structures of bimetallic Pt–Pd particles are based on Monte Carlo simulations using effective-medium potentials.¹⁰ To justify the use of effective-medium potentials for Pt and Pd, we have compared the concentration gradient predicted for the low-index single-crystal surfaces of a 50% Pt: 50% Pd alloy using Monte Carlo simulations based on effective-medium potentials and a total energy calculation based on potentials derived from linear muffin-tin orbital (LMTO) calculations.^{11,12}

II. Experimental Methods

Pt and/or Pd was introduced in the partly dealuminized HY-zeolite (CBV600 from PQ Zeolites BV) by wet impregnation

[†] Haldor Topsøe Research Laboratories.

[‡] Technical University of Denmark.

[⊗] Abstract published in *Advance ACS Abstracts*, February 1, 1997.

TABLE 1: Results of Fitting the EXAFS Data at the Pt L₃-Edge. The Total Metal Load per Gram Catalyst Given in Column 2

Pt:Pd	load, mmol/g	$N_{\text{Pt-Pt}}$	$N_{\text{Pt-Pd}}$	$R_{\text{Pt-Pt}}, \text{\AA}$	$R_{\text{Pt-Pd}}, \text{\AA}$	$\sigma^2_{\text{Pt-Pt}}, \text{\AA}^2$	$\sigma^2_{\text{Pt-Pd}}, \text{\AA}^2$	$\Delta E_{\text{Pt-Pt}}, \text{eV}$	$\Delta E_{\text{Pt-Pd}}, \text{eV}$	χ^2
1:0	0.11	7.3		2.744		0.004		-0.7		0.003
1:1	0.18	8.0	2.8	2.695	2.79	0.005	0.005	-7.7	12.6	0.006
1:2	0.15	7.6	3.4	2.700	2.78	0.004	0.002	-6.5	10.8	0.004
1:3	0.20	7.4	5.4	2.66	2.78	0.005	0.001	-10.8	11.0	0.010
0:1	0.20									

TABLE 2: Results of Fitting the EXAFS Data at the Pd K-Edge. The Particle Size Derived from TEM Measurements as a Volume Average Diameter

Pt:Pd	$D, \text{\AA}$	$N_{\text{Pd-Pd}}$	$N_{\text{Pd-Pt}}$	$R_{\text{Pd-Pd}}, \text{\AA}$	$R_{\text{Pd-Pt}}, \text{\AA}$	$\sigma^2_{\text{Pd-Pd}}, \text{\AA}^2$	$\sigma^2_{\text{Pd-Pt}}, \text{\AA}^2$	$\Delta E_{\text{Pd-Pd}}, \text{eV}$	$\Delta E_{\text{Pd-Pt}}, \text{eV}$	χ^2
1:0	15.4									
1:1	19.4	4.1	4.0	2.741	2.743	0.002	0.0025	0.46	-4.02	0.003
1:2	20.9	4.8	3.6	2.740	2.755	0.003	0.0041	-0.97	-5.2	0.001
1:3	30.1	7.8	1.8	2.755	2.740	0.001	0.002	1.2	4.5	0.002
0:1	31.0	11.0		2.807		0.003		1.51		0.007

using the metal tetraamine-hydrogen carbonates as precursors. After they were dried at about 110 °C, the samples were calcined in air for 2 h at 310 °C and reduced in hydrogen at about 1 bar pressure for 6 h at 300 °C. The composition and total metal load of the samples is given in Table 1. EXAFS experiments were carried out at HASYLABS's RÖMOII beamline at the DESY synchrotron facility in Hamburg, Germany. The storage ring was operated at an energy of 4.552 GeV with a beam current in the interval 80–40 mA. The Si(311)-based monochromator was detuned to about 50% intensity to filter out higher order Bragg scattered beams. Spectra were recorded at the Pt L₃-edge and the Pd K-edge. The samples were placed in an *in situ* cell, reduced for 2 h in a flow of hydrogen at 300 °C, and cooled to room temperature. Three Ar-filled ionization chambers were used to measure the intensity of the X-ray beam. The sample in the *in situ* cell was placed between the first and the second chamber, and a reference compound for energy calibration was placed between the second and the third ionization chamber. Data analysis followed standard procedures.¹³ A linear background, fitted to the preedge region of the spectra, was subtracted from the data followed by edge jump normalization, by change of variable from energy to wavenumber, and by a spline fit subtraction in the EXAFS region. Fourier transformation of the data weighted with a factor k over the interval 2.5–12.5 Å⁻¹ and back-transform over the first coordination shell region 1.2–3.2 Å were applied in order to isolate the EXAFS function for the nearest-neighbor shells only. This function is described by the formula

$$\chi_i(k) = \sum_{j=1}^2 \frac{N_{ij}}{kR_{ij}^2} \times \exp(-\sigma^2 k^2) \times F_j(k) \sin(2kR_{ij} + \Phi_{ij}(k)) \quad (1)$$

The summation is over the two types of neighbors, Pt and Pd. N_{ij} is the number of nearest-neighbors of type j around element i , R_{ij} denotes the bond lengths, σ is the Debye-Waller factor, F_j is the backscattering amplitude, and Φ_{ij} is the absorber-backscatter phase function. The backscattering amplitudes were determined by fitting the EXAFS function of Pt and Pd foils to function 1, treating N_{ij} and R_{ij} as known constants. The phase functions were determined using, in addition to Pt and Pd foils, PdS₂ and PtS₂ references, following the procedure of Sinfelt *et al.*⁷

Transmission electron microscopy (TEM) was carried out on the five different samples after a 6 h reduction in hydrogen at 300 °C. The microscope used was a Philips EM430 operated at 300 kV. Ten images were recorded from each sample, and the diameters of 200–250 particles were measured in order to

give a particle size distribution. The volume averaged diameter for each sample is given in Table 2.

III. Results

Figure 1 shows the experimental EXAFS functions (weighted by k) obtained from the five samples at the Pt L₃-edge (Figure 1a) and the Pd K-edge (Figure 1b). At the Pt L₃-edge, the formation of Pt-Pd alloy particles can be qualitatively identified by the splitting of the peak at about 6 Å⁻¹. This splitting becomes more pronounced with an increasing amount of Pd in the sample. At the Pd K-edge, the alloy formation is seen as a slight shift in the relative intensity between the peaks at about 5.5 and 6.5 Å⁻¹. In the case of pure palladium the peak at 5.5 Å⁻¹ is the more intense, but an increasing amount of platinum in the sample reduces the intensity of this peak. In the 1:1 alloy, the peak at 6.5 Å⁻¹ is slightly more intense than the peak at 5.5 Å⁻¹. The EXAFS functions, obtained after extraction of the contribution from the nearest-neighbor shell, show the same qualitative fingerprints of alloy formation as the complete EXAFS spectra. This is shown in Figure 2 in the case of the 1:2 sample. In Figure 2a, it is clearly shown that the nearest-neighbor contribution at the Pt L₃-edge cannot be adequately described by a single shell of Pt atoms only. Including Pd atoms in the nearest-neighbor shell substantially improves the fit to the data. The same effect is seen in Figure 2b where the nearest-neighbor contribution from the Pd K-edge spectrum cannot be completely described by a shell of Pd atoms only. Inclusion of Pt in the nearest-neighbor shell results in an almost perfect match between the experimental data and a model function of the form of function 1. The result of fitting the first-shell term of the EXAFS functions for each of the five samples to a two-component model function of the form of function 1 is given in Table 1 (for the Pt L₃-edge) and Table 2 (for the Pd K-edge).

IV. *Ab Initio* Calculations of Surface Segregation Profiles

A. Details of the Calculations. In the present work, we have determined the equilibrium concentration profiles of the three low-index surfaces of a random Pt-Pd alloy at a bulk concentration of 50% from first principles. To do so, we used a technique based on a combination of total energy calculations within the framework of density functional theory in the local density approximation (LDA) and statistical mechanics free-energy calculations in the mean-field approximation. The electronic structure and the total energy of the surfaces were calculated by means of the linear muffin-tin orbitals (LMTO) method in conjunction with the coherent potential approximation (CPA) and a Green's function technique.^{11,12,14–20} The complete

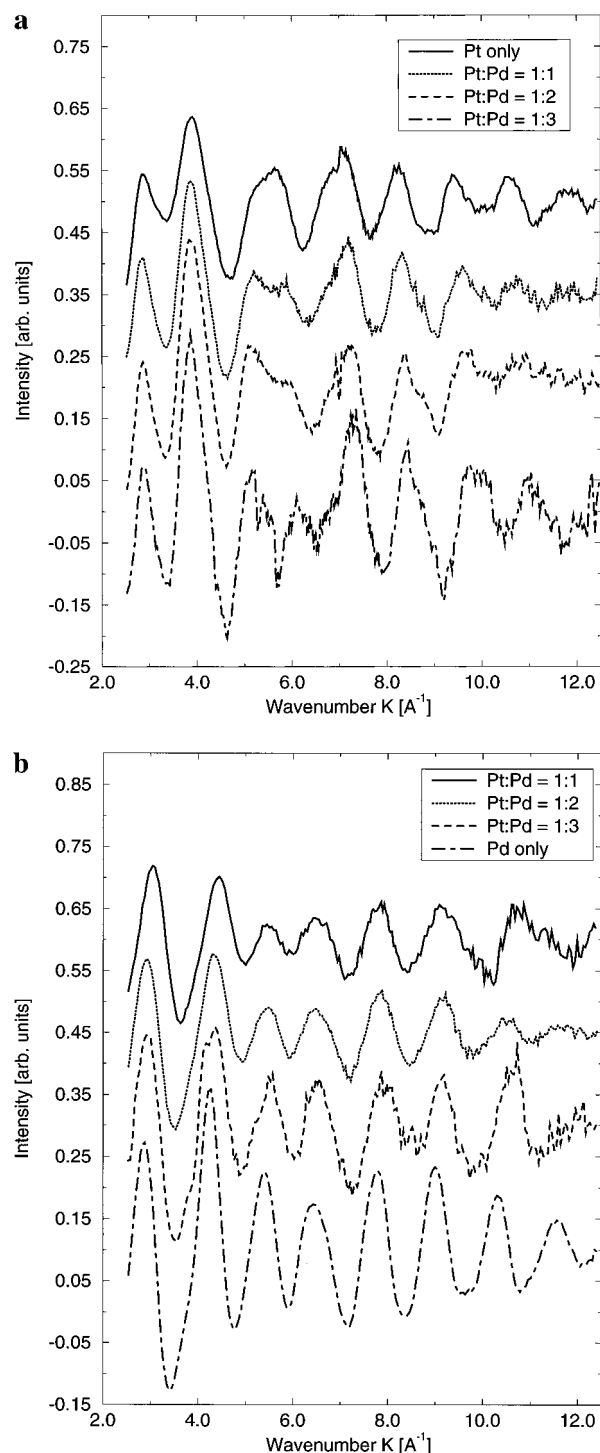


Figure 1. (a) Experimental EXAFS functions at the Pt L₃-edge. (b) Experimental EXAFS functions at the Pd K-edge.

procedure is described in refs 21, 22 where it was used to calculate segregation profiles in CuNi and NiPt. In the present application, the surface region was treated self-consistently and consisted of six layers of atomic spheres and two layers of vacuum spheres. We used the Perdew–Zunger interpolation²³ of the many-body calculations of Ceperley and Alder.²⁴

The equilibrium concentration profile at the surface may be determined by the minimization of the surface free energy of an alloy with respect to a set of the correlation functions $\langle \sigma_{\Lambda,i} \sigma_{\Lambda+k,j} \dots \sigma_{\Lambda+m,l} \rangle$, where $\sigma_{\Lambda,p}$ is the spin variable which takes on the values +1 or -1, depending on the type of atom occupying site p in the layer Λ . Therefore, the concentration of one of the components (Pt in our case) in the layer is then $c_{\Lambda} = (\sigma_{\Lambda} + 1)/2$, where $\sigma_{\Lambda} = \langle \sigma_{\Lambda,p} \rangle$ is the average spin variable

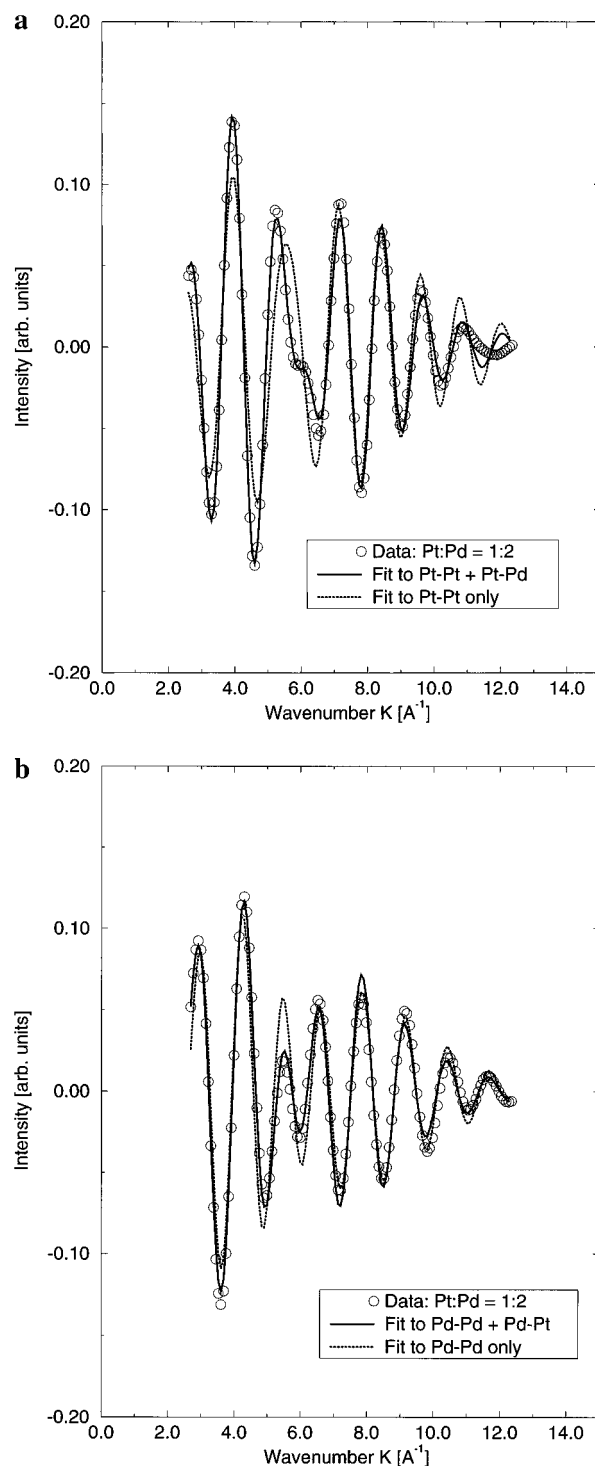


Figure 2. (a) EXAFS functions after extraction of nearest-neighbor shell contribution at the Pt L₃-edge. (b) EXAFS functions after extraction of nearest-neighbor shell contribution at the Pd K-edge.

in the layer. In general, this is a formidable task if one uses a first-principle technique in order to determine the internal energy of the system with a given set of correlation functions. However, it can be greatly simplified by using a parametrization of the surface energy of the system in terms of the interatomic interaction parameters or potentials. For instance, in most cases of fcc transition metal alloys, the overwhelming contribution to the configurational energy comes from the nearest-neighbor interactions. Therefore, all the correlations in the atomic distribution between the sites starting from the second nearest-neighbors can be neglected in such cases and the total energy can be written as:²⁵

$$E_b = E_0 + V_b^{(1)} \langle \sigma_i \rangle + V_b^{(2)} \langle \sigma_i \sigma_j \rangle + V_b^{(3)} \langle \sigma_i \sigma_j \sigma_k \rangle + V_b^{(4)} \langle \sigma_i \sigma_j \sigma_k \sigma_l \rangle \quad (2)$$

Here $V_b^{(1)}$, $V_b^{(2)}$, $V_b^{(3)}$, and $V_b^{(4)}$ are the on-site, pair, triangle, and tetrahedron interactions between nearest-neighbor sites i , j , k , and l . In the case of a completely random alloy, due to the fact that $\langle \sigma_i \sigma_j \dots \sigma_k \rangle = \langle \sigma_i \rangle \langle \sigma_j \rangle \dots \langle \sigma_k \rangle$, the total energy of eq 2 is simplified to the form:

$$E_b^{\text{rand}} = E_0 + \sum_{i=1,4} V_b^{(i)} \sigma^i \quad (3)$$

where $\sigma = \langle \sigma_i \rangle$ is the average spin variable in the alloy.

To determine the surface energy of the alloy with random atomic configuration in each layer parallel to the surface, one has to take into account the fact that both of the interactions and the spin variables depend on the atomic positions relative to the surface:

$$E_{\text{surf}} = \sum_{\Lambda=1}^{\infty} \left[V_{\Lambda}^{(1)} \sigma_{\Lambda} + V_{\Lambda}^{(2)} \sigma_{\Lambda}^2 + V_{\Lambda+}^{(2)} \sigma_{\Lambda} \sigma_{\Lambda+1} + V_{\Lambda++}^{(2)} \sigma_{\Lambda} \sigma_{\Lambda+2} + \dots - \frac{\partial E_b^{\text{rand}}}{\partial \sigma} (\sigma_{\Lambda} - \sigma) \right] \quad (4)$$

Here, the high order terms corresponding to the multiatom interactions are omitted, and $V_{\Lambda}^{(1)}$ and $V_{\Lambda}^{(2)}$ are the on-site and pair interactions in the Λ layer and $V_{\Lambda+}^{(2)}$ is the pair interaction between atoms in the Λ and $\Lambda+1$ layers, and so on.

Formula 4 represents a phenomenological expansion of the surface energy in terms of concentration independent interatomic interactions, which are usually called the Connolly–Williams (CW) interactions.²⁵ To find them, we have calculated the surface energies for some sets of predescribed concentration profiles in the first four layers while the concentration of the fifth and sixth layers were fixed at 50% providing a smooth fit to the bulk region. In total, we treated 32 configurations for the (111) face, 21 for (100) face, and 24 for (110) face. On the basis of these calculations, we have extracted the Connolly–Williams interactions^{21,25} up to a tetrahedra made up of nearest-neighbors by inversion of formula 4. We have checked the convergence of the Connolly–Williams expansion for the bulk Pt–Pd alloys and found that second and other more distant interactions are almost an order of magnitude smaller than those of the nearest-neighbor ones. Therefore, we expect that they are small at the surface as well.

This may not be the case with the *intralayer* interactions for the surface layer $V_{\Lambda}^{(2)}$ which differ even in sign from the corresponding interactions in the second and third layers (*i.e.*, $V_2^{(2)}$ and $V_3^{(2)}$) (see Table 3). But these interactions are not important in the formation of the equilibrium concentration profile, because the concentration profile mainly forms due to the point-energy or on-site interactions $V_{\Lambda}^{(1)}$ and interlayer interactions $V_{\Lambda+}^{(2)}$ and $V_{\Lambda++}^{(2)}$. These interactions, however, are very close to each other for each layer, as one can see in Table 3. Therefore, we may think that interlayer interactions at the surface are very close to those in the bulk, and the most important interactions are the nearest neighbor ones.

Finally, the equilibrium concentration profiles have been calculated within the mean-field approximation for the configurational entropy, neglecting lattice relaxations and any other contributions (*e.g.*, thermal vibrations) to the free energy of the alloy.

TABLE 3: First Several Most Important Interactions in eV for the Low-Index Surfaces of Pt–Pd as Functions of the Layer Number Λ

Surface	Λ	$V_{\Lambda}^{(1)} - V_{\text{bulk}}^{(1)} (=E_{\text{segr},\Lambda}^{\text{Pt}})$	$V_{\Lambda}^{(2)}$	$V_{\Lambda+}^{(2)}$	$V_{\Lambda++}^{(2)}$
(110)	1	0.149	−.003	0.025	0.011
	2	−.046	0.007	0.031	0.009
	3	−0.051	0.010	0.028	0.007
(100)	1	0.129	−.002	0.042	
	2	−.001	0.020	0.030	
	3	−.008	0.018	0.031	
(111)	1	0.066	−0.005	0.046	
	2	0.028	0.021	0.031	
	3	−.001	0.019	0.030	

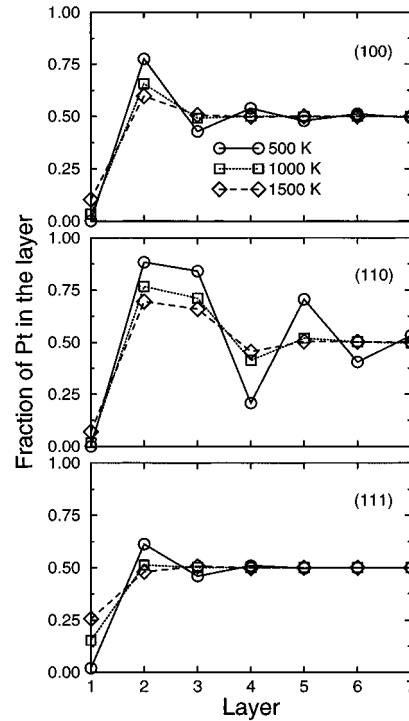


Figure 3. Segregation profiles obtained from the LMTO calculations for the three low-index faces of disordered $\text{Pt}_{50}\text{Pd}_{50}$. Full line and dotted and dashed lines are the results for 500, 1000, and 1500 K, correspondingly.

B. Results. The calculated surface concentration profiles for the three low-index surfaces of $\text{Pt}_{50}\text{Pd}_{50}$ random alloys at 500, 1000, and 1500 K are shown in Figure 3. The results show oscillatory surface-concentration profiles for all three faces, and in all cases we find that Pd segregates toward the surface. Therefore, at 500 K and below this temperature, all these faces will be covered by Pd atoms. All these trends can be easily explained by considering obtained CW interactions presented in Table 3.

For instance, the segregation energy in the Λ layer according to the definition is

$$E_{\text{segr},\Lambda}^{\text{Pt}} = \frac{\partial E_{\text{surf}}}{\partial \sigma_{\Lambda}} (= -E_{\text{segr},\Lambda}^{\text{Pd}}) \quad (5)$$

where the derivative is taken at a given fixed concentration profile. For an unsegregated alloy at the equiatomic alloy composition, when $\sigma_{\Lambda} = \sigma = 0$, one finds

$$E_{\text{segr},\Lambda}^{\text{Pt}} = -E_{\text{segr},\Lambda}^{\text{Pd}} = V_{\Lambda}^{(1)} - V_b^{(1)} \quad (6)$$

Thus, in Table 3 one can find that segregation energies of Pd are −0.149, −0.129, and −0.066 eV in the first layer of (110), (100), and (111) surfaces, correspondingly. They are

greater than the energies of other interactions; therefore at ambient temperatures all three faces should consist of mainly Pd atoms. The segregation energies of Pt in the second and third layers of the (110) surface are great enough to explain the enrichment of Pt in the layers as seen in Figure 3.

In the case of (111) and (100) surfaces, however, the values of the segregation energies in the second and third layers are of the same order or even less than the values of those of the pair interactions $V_{\Lambda}^{(2)}$ and $V_{\Lambda+1}^{(2)}$, which are responsible for the ordering effects in the system (for instance, if $V_{\Lambda+1}^{(2)}$ is positive the surface energy of the system will be the lowest for alternate compositions in the Λ and $\Lambda+1$ layers, i.e., Pd–Pt or vice versa). That is why, despite the fact that the segregation energy of Pt is positive in the second layer of the (111) surface, Pt does go to this layer at low temperatures: there should be Pd in the first layer and the ordering energy between the first and second layer, which roughly corresponds to $V_{\Lambda+1}^{(2)}$, is greater than $V_2^{(1)}$. Thus, the Pt enrichment of the second layer of (111) surface is the consequence of the frustration effect due to the competition between interlayer ordering and intralayer segregation. In the case of NiPt(110) this leads to the segregation reversal in the surface layer.²² A similar explanation may be given for the enrichment of Pt in the third layer of the (110) surface. It also means that actually both the segregation of Pd towards the first layer and Pt enrichment of the second layer are relatively less stable processes than the segregations at the other faces. One can see, for instance in Figure 3, that the temperature dependence of the composition of the first two layers in the case of the (111) surface is stronger than that in the others; therefore, at 1500 K there is even a small Pd enrichment in the second layer. Finally, we would like to point out that these fragile equilibria at the (111) surface can be easily disturbed. For example, an adsorbed molecule which interacts more strongly with Pt than with Pd may cause a surface segregation reversal.

V. Monte Carlo Simulations of Segregation

A. Low-Index Surfaces. In order to calculate the segregation in small particle Pt–Pd alloys, we have calculated the interatomic interactions by means of effective-medium potentials.¹⁰ Monte Carlo simulations were used to obtain equilibrium properties at finite temperatures. The parameters in the EMT potentials for Pt and Pd were taken from²⁶ and subsequently adjusted such that the simulated segregation profiles of the three low-index faces correspond with the results obtained from the *ab initio* calculations shown in Figure 3.

Slab calculations for the three low-index surfaces were performed for a box of 15 layers parallel to the surface with 5×5 atoms per layer for the ratio of Pd:Pt = 1. Atoms in the upper 10 layers were allowed to swap their labels in a Monte Carlo scheme. The atoms in the lower 5 layers were fixed to mimic a 50% random bulk alloy. No vibrations or relaxations were allowed, in order to compare the EMT results directly to the *ab initio* calculations. The initial positions of the Pt and Pd atoms were chosen randomly on a fcc lattice with a lattice constant corresponding to the linear interpolation between the Pt and Pd bulk lattice constants. The interaction range of the effective-medium potentials was cut off between the third and fourth nearest-neighbor distance. After equilibration, 25 snapshots (spaced with 10 snapshots) were used to calculate the concentration profiles perpendicular to the surface. The concentration profiles at 500 K are shown in Figure 4. A comparison of this figure with the segregation profiles calculated by the *ab initio* potentials (Figure 3), shows a rough overall agreement for all three low-index faces. Inspection of the

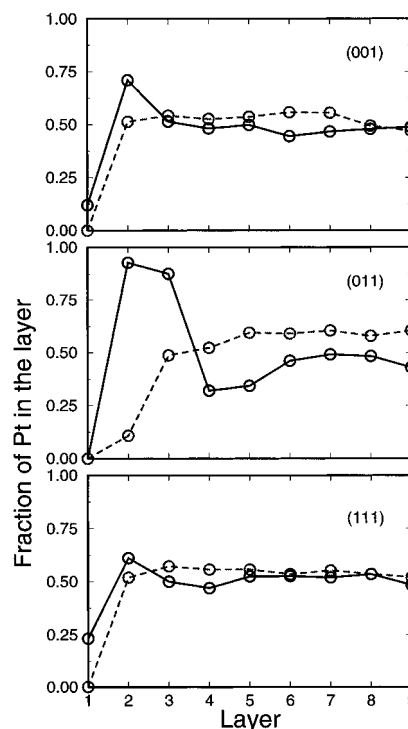


Figure 4. Calculated equilibrium segregation profiles for the three low-index surfaces of Pt–Pd 50% random alloys. The atomic fraction of Pt is shown at 500 K, using the original EMT-values for V_0 for Pt ($V_0 = 4.067$ eV) (solid curve). The dashed curve shows the segregation profile for the adapted Pt potential ($V_0 = 8.124$ eV). Layer 1 corresponds to the surface layer.

TABLE 4: Segregation Energies (in eV) for a Pt Impurity in the Low-Index Pd Faces and a Pd Impurity in the Low-Index Pt Faces Obtained from EMT and LMTO

		EMT	LMTO
Pt Impurity in	Pd(111)	+0.07	+0.24
	Pd(001)	+0.10	+0.36
	Pd(011)	+0.14	+0.42
Pd Impurity in	Pt(111)	−0.03	+0.08
	Pt(001)	−0.06	−0.12
	Pt(011)	−0.09	−0.06

profiles in close detail reveals that the segregation of Pd to the surface as calculated from the effective-medium theory is less strong than the Pd segregation obtained from the LMTO calculations.

The underestimation of the segregation of Pd can also be observed in the segregation energies of a Pt impurity in Pd (see Table 4). The segregation energies of impurities were determined by comparing the energy of a single Pt impurity in a Pd bulk with the energy of a single Pt impurity at the surface of a low-index Pd face. The atomic positions were relaxed, starting from perfect fcc positions, according to a molecular-dynamics minimization procedure.

From this comparison between LMTO and EMT, we have to conclude that, although the trend in the Pd segregation for the low-index surfaces is given correctly by the EMT, the magnitude of the segregation is underestimated. A similar conclusion can be drawn by comparing the difference in surface free energies of Pd(111) and Pt(111) surfaces. Jacobsen *et al.*²⁶ showed that the EMT not only strongly underestimates the surface free energies of Pd(111) and Pt(111), but the difference in free energies between these two surfaces as well, in comparison with experimental data.

In order to use the effective-medium potential to simulate the segregation in nanoparticle Pt–Pd clusters, we have adjusted

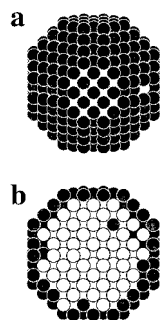


Figure 5. (a) Projected snapshot of an equilibrated Pt–Pd cluster (Pd:Pt = 1, $M = 675$ atoms, $T = 300$ K). (b) Same snapshot sliced through the center. The dark circles are Pd atoms, the white circles Pt.

one parameter (V_0) in the pair-potential part of the atomic sphere correction, such that the segregation profiles for the low-index surfaces match the LMTO results reasonably well (see the dashed curves in Figure 4). Although the agreement is not quantitatively correct, the essential feature that there is no Pt in the surface layer is simulated properly by this adapted EMT potential. At the (011) surface, the adjustment of V_0 leads to an overestimation of the Pd segregation. This will not have a significant influence on the segregation in the particles, because (011) surfaces are hardly present here. Because the shear modulus C_{44} is linearly dependent on V_0 , it will be doubled as well. This will not affect any results if relaxation of atomic positions is disallowed.

B. Segregation in Nanoclusters. The segregation in small clusters has been simulated, using the effective-medium theory to calculate the interatomic interactions and the Monte Carlo technique to obtain thermodynamic equilibrium properties. Pt and Pd atoms were placed randomly on a fcc lattice for the initial configuration. The lattice constant corresponds to the interpolation, linearly weighted by the Pd:Pt ratio, between the Pt and Pd bulk lattice constants. The shape of a cluster was chosen as a spherically truncated nucleus. Four different cluster diameters were simulated: 11.7 Å ($M = 55$ atoms), 19.5 Å ($M = 249$ atoms), 26.5 Å ($M = 675$ atoms), and 35.1 Å ($M = 1505$ atoms). The Pd:Pt concentrations were chosen equal to the ratios used in the EXAFS experiments: Pd:Pt = 1, Pd:Pt = 2, and Pd:Pt = 3. The equilibration of the clusters was performed at constant temperature T , constant number of atoms, and at a constant Pd:Pt concentration in a Monte Carlo scheme which allowed for swaps of atoms.

In order to compare the simulation results to the EXAFS experiments, the coordination numbers $N_{\text{Pt-Pt}}$, $N_{\text{Pt-Pd}}$, $N_{\text{Pd-Pt}}$, and $N_{\text{Pd-Pd}}$ were computed as the average coordination numbers over an ensemble of 25 snapshots. The snapshots were produced after a cluster was equilibrated and 10 Monte Carlo cycles were chosen in between to obtain statistically independent configurations. In one Monte Carlo cycle M , attempts to swap the labels of two different atoms are made; here M is the total number of atoms in the cluster. The coordination numbers were counted for every atom in the cluster, and subsequently the average coordination number N_{ij} ($i, j = \text{Pt, Pd}$) was computed as the average over all atoms in the cluster. The resulting coordination numbers for $T = 300$ K and Pd:Pt = 1 are shown in Figure 6 as a function of cluster diameter. Similar simulations were performed for Pd:Pt = 2 and Pd:Pt = 3. Visual inspection of equilibrated clusters shows that Pd always segregates to the surface (Figure 5).

In order to get insight into the variation of the coordination numbers with cluster size, the coordination numbers for two different models are shown in Figure 6 as well. Putting Pt and Pd atoms randomly on a fcc lattice results in equal averages

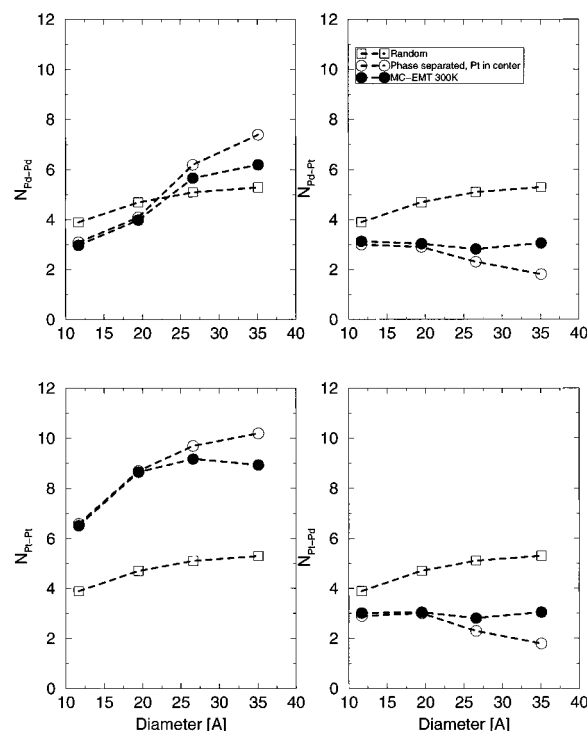


Figure 6. Coordination numbers as a function of cluster diameter for spherically truncated fcc clusters with Pd:Pt = 1 (see text).

TABLE 5: Particle Size Distributions Obtained from TEM for Pd:Pt Ratios Used in EXAFS Experiments

$D, \text{\AA}$	volume fraction of atoms in clusters within D				
	Pd:Pt = 0	Pd:Pt = 1	Pd:Pt = 2	Pd:Pt = 3	Pd:Pt = ∞
5–10	0.007	0.000	0.000	0.000	0.000
10–15	0.442	0.069	0.044	0.000	0.000
15–20	0.500	0.527	0.429	0.036	0.008
20–25	0.051	0.356	0.384	0.299	0.111
25–30	0.000	0.048	0.101	0.430	0.260
30–35	0.000	0.000	0.043	0.163	0.252
35–40	0.000	0.000	0.000	0.071	0.254
40–45	0.000	0.000	0.000	0.071	0.082

for all four coordination numbers (Figure 6, \square). Phase separation with Pt in the center and Pd at the surface of the cluster results in high $N_{\text{Pt-Pt}}$ and relatively low $N_{\text{Pd-Pd}}$ (Figure 6, \circ).

As all coordination numbers are dependent on the cluster size, a proper average value has to be calculated for a reliable comparison between the EMT simulations and the EXAFS experiments. Particle size distributions for the samples of different Pd:Pt ratios were obtained by TEM and are shown in Table 5. All coordination numbers in Figure 6 were averaged over the particle size distributions listed in Table 5, and the resulting coordination numbers are shown as a function of Pd:Pt ratio in Figure 7. The results of the EXAFS analysis are shown as well.

The EXAFS data were compared to the models by means of a χ^2 analysis. Here $\chi^2 = (1/P\sigma) \sum_{i=1}^P (N_{i,\text{EXAFS}} - N_{i,\text{model}})^2$, with P the total number of points and σ the average error bar of the experimental data. Summing χ^2 for all four permutations of Pt and Pd, and estimating $\sigma = 1$, leads to the χ^2 -values shown in Table 6. It is clearly seen that both models with Pd at the surface describe the experimental data closely, and within the error bar we cannot distinguish between them. The results from the adapted EMT potential follow the data very closely as well.

VI. Discussion

The most noticeable result of the EXAFS fits given in Tables 1 and 2 is the rather high value of $N_{\text{Pt-Pt}}$ for all the bimetallic

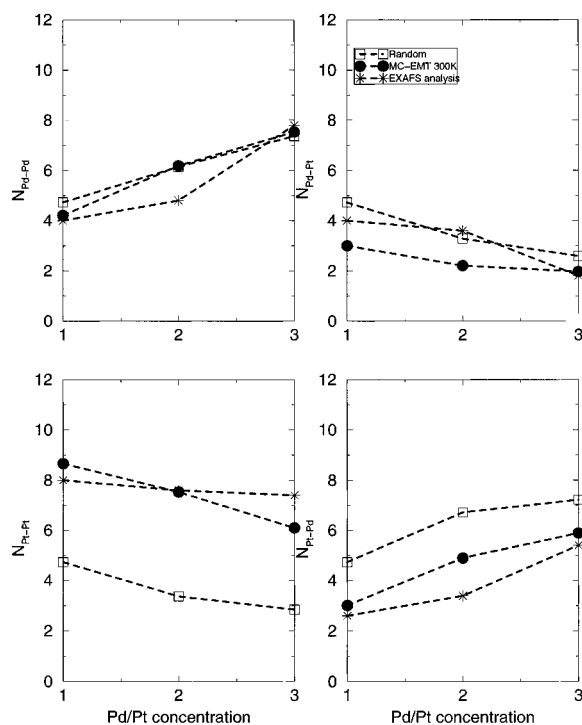


Figure 7. Coordination numbers averaged over experimentally obtained particle size distributions as a function of the Pd:Pt ratio.

TABLE 6: χ^2 Analysis of the Coordination Numbers

χ^2	model
0.8	MC-EMT 300 K, V_0 Pt = 8.124 eV (adapted value for V_0)
1.2	1 monolayer Pd at the surface, random alloy inside
1.6	phase separated with Pt in the center and Pd at the surface
4.8	MC-EMT 300 K, V_0 Pt = 4.067 eV (value from V_0 in original EMT theory)
5.7	random Pt–Pd alloy
6.4	1 monolayer Pt at the surface; random alloy inside
6.9	phase separated by a plane parallel to a plane through center

samples, especially when compared to the value of $N_{\text{Pd-Pd}}$. This points very strongly to some kind of separation of Pt and Pd in the small particles. Considering the 1:1 sample random alloying would manifest itself in four equal coordination numbers. A Pt core surrounded by a shell of Pd would, however, give rise to $N_{\text{Pt-Pt}}$ being greater than $N_{\text{Pd-Pd}}$. Such a model of the elemental distribution in the small particles is consistent with the calculations in section IV of this paper and with experimental measurements of Pd segregation in single-crystal Pt–Pd alloys.²⁷

There are, however, a few other effects that could lead to $N_{\text{Pt-Pt}} > N_{\text{Pd-Pd}}$. Anharmonicity of the atomic potentials have recently been shown to cause an underestimation of the coordination number for small particles of Cu²⁸ while the effect in Pt particles was found to be small. Assuming that anharmonic effects are more important for Pd than for Pt, we estimate on basis of the results given in ref 28 that the values of $N_{\text{Pd-Pd}}$ could be underestimated by 0.5 units at the most. Thus, anharmonic effects are not the reason for the high values of $N_{\text{Pt-Pt}}$ and the low values of $N_{\text{Pd-Pd}}$. A more serious point is the observation in TEM of a few rather large (about 100 nm in size) Pt rich metal particles on the outer surface of zeolite grains. Such particles were found in all Pt-containing samples. However, H_2 -TPD measurements²⁹ of the 5 samples show dispersions in good agreement with the average particle sizes measured in TEM (i.e., in the range 50–90%). Since 20–40% of the Pt atoms would have to be present in large particles in order to bring $N_{\text{Pt-Pt}}$ up to the value of 8 in a random alloy model, we also disregard this possibility as the explanation for the high

values of $N_{\text{Pt-Pt}}$ in our EXAFS analysis. Smaller variations in the composition of the individual bimetallic particles may occur, however. Especially in the sample with Pd:Pt = 3:1, the relatively large value of $N_{\text{Pd-Pd}}$ indicate that particles of pure Pd may have formed.

The evaluation of the different models of the Pt–Pd distribution in the bimetallic particles shown in Table 4, clearly favors models based on segregation of Pd to the surface of the small particles. Changing the assumption of truncated octahedral shape of the particles to hemispherical particles, for example, does not change this result. Even when the first one or two layers in contact with the support is assumed to be pure Pt, the model must include Pd segregation in order to reproduce the EXAFS data. It is difficult, however, from the experimental data to discriminate between the various models including Pd segregation (i.e., it is difficult to conclude whether there is a tendency for segregation in other layers than the surface layer).

In assessing the effect of alloy formation and surface enrichment with Pd on the catalytic properties of the Pt–Pd catalysts, we have to keep in mind that the present EXAFS experiments were carried out in a hydrogen atmosphere. Since the binding energy of hydrogen to Pt and Pd is almost the same^{30,31} we have neglected the effects of adsorbates on the segregation properties of the small bimetallic particles. This could still make our results of relevance for hydrogenation reactions of pure hydrocarbon (e.g., hydrogenation of benzene to cyclohexane or acetylene to ethane). In hydrogenation reactions of oil feeds the presence of sulfur compounds leads to adsorption of sulfur on the surface of the bimetallic particles. Since the binding of S to Pd is stronger than the binding to Pt, the stability of the bimetallic particles in the presence of sulfur compounds like H_2S may be questioned. The same could be the case for oxidation reactions and reactions involving CO. Another question related to the catalytic properties of the bimetallic particles is the influence of alloy formation and surface segregation on the electronic properties which govern the reactivity of these metals. Recent calculations³² estimate these effects to be small. Hence, we would not expect very strong synergetic effects in the catalytic properties of Pt–Pd alloys.

VII. Conclusions

We have shown that small zeolite-supported bimetallic Pt–Pd particles can be prepared by standard impregnation techniques. In a hydrogen atmosphere, the surface of the bimetallic particles are strongly enriched in Pd. This is in agreement with LMTO calculations of segregation profiles of low-index single-crystal alloy surfaces. EMT potentials of Pt and Pd can be modified such that reasonable agreement with LMTO results on segregation profiles can be obtained. Monte Carlo simulations based on adjusted EMT potentials predict strong surface segregation of Pd in small bimetallic Pt–Pd particles. Coordination numbers derived from such simulations are in good agreement with those derived from EXAFS measurements of three bimetallic zeolite-supported Pt–Pd catalysts. The theoretical methods developed in this work may be applied to other bimetallic systems to predict the segregation effects in small bimetallic particles.

Acknowledgment. We gratefully acknowledge Hasyllab at DESY for providing synchrotron beam time at the RÖMO II beamline. This work has been financed by the Danish Natural Science Research Council. The Center for Atomic-scale Materials Physics is sponsored by the Danish National Research Foundation. We are indebted to Dr. B. S. Clausen for providing

us with the software for the EXAFS data analysis and Dr. I. A. Abrikosov for helping with the calculations of the surface energies. Prof. J. K. Nørskov, Dr. H. Skriver, and Dr. B. S. Clausen are greatly thanked for many stimulating discussions. We also thank G. Steffensen for his participation in collecting the EXAFS data.

References and Notes

- (1) Twigg, M. V., Ed. *Catalyst Handbook* Wolfe Publishing Ltd.: U.K., 1989.
- (2) Stanislaus, S. A.; Cooper, B. H. *Catal. Rev. Sci. Eng.* **1994**, *36*, 75.
- (3) Hammer, B.; Scheffler, M. *Phys. Rev. Lett.* **1995**, *74*, 3487.
- (4) Hammer, B.; Nørskov, J. K. *Nature* **1995**, *376*, 238.
- (5) Xu, C.; Koel, B. *Surf. Sci.* **1994**, *304*, 249.
- (6) Xu, C.; Koel, B. *Surf. Sci. Lett.* **1994**, *304*, 1505.
- (7) Sinfelt, J. H.; Via, G. H.; Lytle, F. W. *Catal. Rev. - Sci. Eng.* **1984**, *26*, 81.
- (8) Sinfelt, J. H. *Bimetallic Catalysts*; Exxon Monograph; J. Wiley & Sons Inc.: New York, 1983.
- (9) Toshima, N. *et al. J. Phys. Chem.* **1991**, *95*, 7448.
- (10) Jacobsen, K. W.; Nørskov, J. K.; Puska, M. J. *Phys. Rev. B: Condens. Matter* **1987**, *35*, 7423.
- (11) Andersen, O. K. *Phys. Rev. B* **1975**, *12*, 3060.
- (12) Skriver, H. L. *The LMTO Method*; Springer-Verlag: Berlin, 1984.
- (13) Teo, B. K. *EXAFS: Basic Principles and Data Analysis*; Springer-Verlag, Berlin, 1986.
- (14) Gunnarsson, O.; Jepsen, O.; Andersen, O. K. *Phys. Rev. B: Condens. Matter* **1983**, *27*, 7144.
- (15) Andersen, O. K.; Jepsen, O. *Phys. Rev. Lett.* **1984**, *53*, 2571.
- (16) Andersen, O. K.; Jepsen, O.; Glötzl, D. In *Highlights of Condensed-Matter Theory*; Eds. Bassani, F.; Fumi, F.; Tosi, M. P., Eds.; North Holland: New York, 1985.
- (17) (a) Andersen, O. K.; Pawłowska, Z.; Jepsen, O. *Phys. Rev. B: Condens. Matter* **1986**, *34*, 5253. (b) Andersen, O. K.; Pawłowska, Z.; Jepsen, O. Private communication.
- (18) Lambrecht, W. R. L.; Andersen, O. K. *Surf. Sci.* **1986**, *178*, 256.
- (19) Skriver, H. L.; Rosengaard, N. M. *Phys. Rev. B: Condens. Matter* **1991**, *43*, 9538.
- (20) Abrikosov, A. I.; Skriver, H. L. *Phys. Rev. B: Condens. Matter* **1993**, *47*, 16532.
- (21) Ruban, A. V.; Abrikosov, I. A.; Ya Kats, D.; Gorelikov, D.; Jacobsen, K. W.; Skriver, H. L. *Phys. Rev. B: Condens. Matter* **1994**, *49*, 11383.
- (22) Abrikosov, I. A.; Ruban, A. V.; Skriver, H. L.; Johanson, B. *Phys. Rev. B: Condens. Matter* **1994**, *50*, 2039.
- (23) Perdew, J. P.; Zunger, A. *Phys. Rev. B: Condens. Matter* **1981**, *23*, 5048.
- (24) Ceperley, D. M.; Alder, B. J. *Phys. Rev. Lett.* **1980**, *45*, 566.
- (25) Connolly, J. W. D.; Williams, A. R. *Phys. Rev. B: Condens. Matter* **1983**, *27*, 5169.
- (26) Jacobsen, K. W.; Stoltze, P.; Nørskov, J. K. *Surf. Sci.* **1996**. Accepted for publication.
- (27) Kuijers, F. J.; Tiemar, B. M.; Ponec, V. *Surf. Sci.* **1978**, *75*, 657.
- (28) Clausen, B. S.; Gråbæk, L.; Topsøe, H.; Stoltze, P.; Hansen, L. B.; Nørskov, J. K.; Nielsen, O. H. *J. Catal.* **1993**, *141*, 368.
- (29) Hansen, P. L.; Tkachenko, O.; Shpiro, E.; Borovkov, V.; Dimitriev, R. **1997**, in preparation.
- (30) Lisowski, W. *Appl. Surf. Sci.* **1988**, *31*, 451.
- (31) Dus, R.; Lisowski, W. *Surf. Sci.* **1986**, *59*, 141.
- (32) Ruban, A. V.; Hammer, B.; Stoltze, P.; Skriver, H. L.; Nørskov, J. K. *J. Mol. Catal.* **1996**, Accepted for publication.